

# Probabilistic Localization of Insect-Scale Drones on Floating-Gate Inverter Arrays

Priyesh Shukla<sup>1</sup>, *Student Member, IEEE*, Ankith Muralidhar<sup>1</sup>, Nick Iliev<sup>1</sup>, Theja Tulabandhula<sup>2</sup>, Sawyer B. Fuller<sup>3</sup> and Amit Ranjan Trivedi<sup>1</sup>, *Member, IEEE*

**Abstract**—We propose a novel compute-in-memory (CIM)-based ultra-low-power framework for probabilistic localization of insect-scale drones. Localization is a critical subroutine for path-planning and rotor control in drones, where a drone is required to continuously estimate its pose (position and orientation) in flying space. The conventional probabilistic localization approaches rely on the three-dimensional (3D) Gaussian Mixture Model (GMM)-based representation of a 3D map. The GMM map model is synthesized by scanning the 3D space and by modeling the density of matter. A GMM model with hundreds of mixture functions is typically needed to adequately learn and represent the intricacies of the map. Meanwhile, localization using complex GMM map models is computationally intensive. Since insect-scale drones operate under extremely limited area/power budget, continuous localization using GMM models entails much higher operating energy – thereby, limiting flying duration and/or size of the drone due to a larger battery. Addressing the computational challenges of localization in an insect-scale drone using a CIM approach, we propose a novel framework of 3D map representation using a harmonic mean of “Gaussian-like” mixture (HMGM) model. We show that *short-circuit current* of a multi-input floating-gate CMOS-based inverter follows the harmonic mean of a Gaussian-like function. Therefore, the likelihood function useful for drone localization can be efficiently implemented by connecting many multi-input inverters in parallel, each programmed with the parameters of the 3D map model represented as HMGM. When the depth measurements are projected to the input of the implementation, the summed current of the inverters emulates the likelihood of the measurement. We have characterized our approach on an RGB-D indoor localization dataset. The average localization error in our approach is  $\sim 0.1125$  m which is only slightly degraded than software-based evaluation where the average localization error is  $\sim 0.08$  m. Meanwhile, our localization framework is ultra-low-power, consuming as little as  $\sim 17$   $\mu$ W power while processing a depth frame in 1.33 ms over hundred pose hypotheses in the particle-filtering (PF) algorithm used to localize the drone. Comparatively, a custom-designed 8-bit digital processor requires  $\sim 7.6$  mW power for the same workload. Therefore, the proposed approach consumes  $\sim 450\times$  less energy than the traditional, paving the way for tiny autonomous drones.

**Index Terms**—Compute-in-memory (CIM), insect-scale drones, probabilistic localization.

## I. INTRODUCTION

Spatially intelligent devices can autonomously traverse and explore their application domain, thereby, opening intriguing prospects for sensors and embedded systems. For example,

The authors are with <sup>1</sup>Department of Electrical and Computer Engineering, University of Illinois at Chicago, IL 60607 USA, <sup>2</sup>Department of Information and Decision Sciences, University of Illinois at Chicago, IL 60607 USA, and <sup>3</sup>Department of Mechanical Engineering, University of Washington, Seattle, WA 98115 USA.

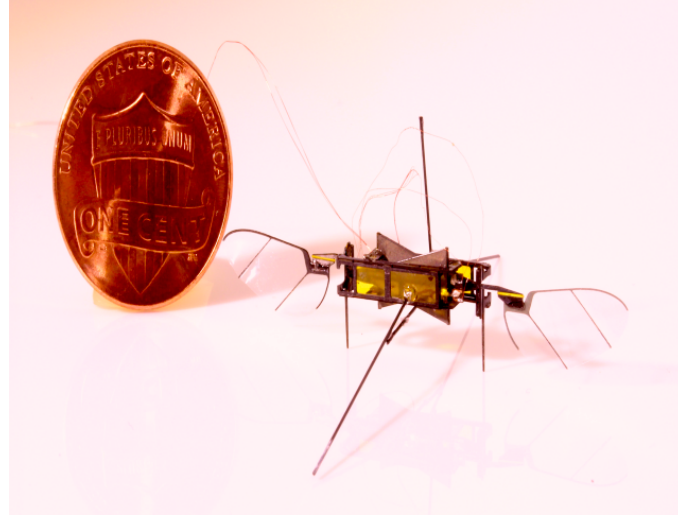


Fig. 1: Insect-scale drone [12] weighing less than a gram and smaller than a penny was demonstrated by Fuller lab in the University of Washington.

in an agriculture field, flying cameras can locate infected plants to prevent disease spread [1], [2]; flying gas sensors can identify gas leaks in an industrial plant [3], [4]; during earthquakes, autonomous cameras can assist in search and rescue missions by navigating through building debris [5], [6]; and inside a home, a flying camera can actively monitor fire breakouts and intruders [7], [8]. Thus, most embedded systems, enlivened by spatial intelligence, can have dramatically elevated use-cases. However, the flying devices must also be small enough to be non-intrusive to people in the flying spaces and be able to navigate through constricted spaces. Recently, impressive progress has been made in miniaturizing drones. So called *insect-scale drones* studied in [9]–[12] weigh less than a gram and are smaller than a penny. Meanwhile, since an insect-scale drone can only carry the payload of a tiny battery, minimizing power dissipation of on-board processing for spatial intelligence becomes extremely critical [13]. While the cloud can be leveraged to circumvent the above on-board processing challenges, in many applications, reliable continuous connectivity to the cloud cannot be assumed. Cloud-based control may also suffer from unpredictable latency. Moreover, continuous transmission of drone’s video stream to cloud itself is energy hungry [14]. Hence, on-board ultra-low-power processing capacity for self-navigation is indispensable.

The *most basic operation* for self-navigation is to determine the position and orientation (i.e., pose) of a drone during its flight. Path planning objectives such as motion tracking and obstacle avoidance require one to continuously assess

the drone’s pose. Therefore, drone localization must also be evaluated in real-time. Additionally, since the flying space of a drone is dynamic, drone localization must be robust against dynamic variations in the flying space. For example, in an indoor application, there will be movement of people and changes in lighting conditions. Localization of a drone must be robust against these variations. Bayesian probabilistic inference is a promising approach for enhancing the robustness of inference by extracting both the prediction and the *confidence* of prediction [15]–[17]. A probabilistic framework for drone localization models the likelihood of measurement against a hypothesized drone’s pose model [18]. The posterior probability of drone’s pose can be compared against competing hypotheses to identify the most likely one. The likelihood models can also estimate the prediction confidence based on the variance of the prediction. A high confidence prediction will have low variance in estimates, and *vice versa*. Nonetheless, current state-of-the-art probabilistic localization models are quite computationally intensive. While predictive robustness of a probabilistic localization is highly desirable in an insect-scale drone, incorporating the same is quite challenging due to limited computational resources as well as the need to predict in the real-time. Overcoming the above challenges, this work makes the following key contributions:

- We propose a novel representation of 3D maps using a harmonic mean of “Gaussian-like” mixture (HMGM) model. We show that, unlike a Gaussian Mixture Model (GMM), HMGMs can be computed with much higher efficiency and enable a similar localization accuracy as GMM. We also discuss an Expectation Maximization (EM)-based learning procedure for HMGM’s extraction.
- We use the key property that the short-circuit current of a multi-input floating gate CMOS inverter circuit follows the harmonic mean of Gaussian-like functions. Therefore, by emulating the key computing kernels in our localization approach directly at the transistor level, we are able to minimize computing workload and data movements in the processing, and thereby, energy demand for the computing. Using the proposed implementation, the localization model is evaluated with high parallelism, therefore, timing and energy constraints for real-time predictions that were hard to achieve are now feasible.
- We have characterized our localization approach using an RGB-D dataset. The average localization error in our hardware-based approach is  $\sim 0.1125$  m which is only slightly worse than software-based error, viz.,  $\sim 0.08$  m. Our localization framework, meanwhile, is ultra-low-power. Our approach consumes  $\sim 17$   $\mu$ W power when processing a depth frame in 1.33 ms over hundred pose hypotheses using particle-filtering (PF). Comparatively, a custom-designed 8-bit digital processor consumes  $\sim 7.6$  mW power which is  $450\times$  higher than our approach. We have also rigorously analyzed the impact of process variability and limited precision in our design, and document methodologies to mitigate their impact.

## II. OVERVIEW OF PROBABILISTIC LOCALIZATION

Localization of an autonomous mobile agent invites uncertainties in its pose estimates. A probabilistic localization framework can rigorously account for such modeling and measurement uncertainties to not only predict the estimated pose but also the *confidence* of prediction, which is expressed by the variance of the predicted estimate. Extracting prediction confidence along with the prediction itself allows for a *risk-aware* navigation, wherein the drone can seek additional measurements if the prediction confidence is low.

Using Bayes’ rule, the posterior probability of pose ( $\mathbf{x}$ ) of a drone is given by

$$P(\mathbf{x}|\mathbf{z}) = \frac{P(\mathbf{z}|\mathbf{x})P(\mathbf{x})}{P(\mathbf{z})} \quad (1)$$

Here,  $P(\mathbf{z}|\mathbf{x})$  is the likelihood of measurement  $\mathbf{z}$  and  $P(\mathbf{x})$  is the prior probability of pose belief. A maximum likelihood estimate (MLE) of drone’s pose maximizes the likelihood of the current measurement, i.e.,

$$\mathbf{x}_{\text{MLE}} = \text{argmax} P(\mathbf{z}|\mathbf{x}) \quad (2)$$

Meanwhile, the maximum a posteriori estimate (MAP) of pose searches for the estimate that maximizes posterior probability of the pose, i.e.,

$$\mathbf{x}_{\text{MAP}} = \text{argmax} P(\mathbf{z}|\mathbf{x})P(\mathbf{x}) \quad (3)$$

Under global localization, when the drone is completely uncertain about its pose, MAP and MLE are equivalent. Otherwise, MAP estimate allows for a systematic way to account for prior belief. Using probabilistic localization, a drone can also recursively integrate sequential measurements in a systematic framework to reduce its estimation uncertainties. *Bayesian filtering* [19] is a well-established localization method for this purpose where the belief of drone’s pose can be estimated using a recursive flow of Bayes’ rule as

$$\overline{bel}(\mathbf{x}_t) = \sum_{\mathbf{x}_{t-1}} P(\mathbf{x}_t|\mathbf{u}_t, \mathbf{x}_{t-1})\overline{bel}(\mathbf{x}_{t-1}) \quad (4a)$$

$$\overline{bel}(\mathbf{x}_t) = \eta P(\mathbf{z}_t|\mathbf{x}_t)\overline{bel}(\mathbf{x}_t) \quad (4b)$$

Here,  $\overline{bel}(\mathbf{x}_t)$  in (4a) is the drone’s new pose belief at iteration ‘ $t$ .’  $\overline{bel}(\mathbf{x}_{t-1})$  is the pose belief at previous iteration ‘ $t - 1$ .’  $\mathbf{u}_t$  is the control input to the drone.  $P(\mathbf{x}_t|\mathbf{u}_t, \mathbf{x}_{t-1})$  is the probabilistic motion model exploiting Markov assumption where belief of  $\mathbf{x}_t$  depends only on the previous state’s belief, and the most recent control signal  $\mathbf{u}_t$ . (4b) is the correction on the new pose belief based on the sensor measurements.

Particle Filtering [20], [21] allows a practical implementation of Bayesian filtering under arbitrary likelihood and belief function profiles by using a Monte Carlo method. Instead of relying on analytically defined likelihood and belief functions, the method considers a set of hypotheses (aka particles) sampled based on the underlying density functions. Each particle has an associated weight index which is updated based on the measurements following the above equations. Unlikely particles with low likelihood are sequentially filtered out with each measurement. Various uncertainties, such as in drone’s motion control, are accounted for by regenerating a new particle set from the current, where children particles represent stochastic deviations corresponding to motion control uncertainties.

Although Bayes’ rule-based probabilistic localization allows a systematic framework to seamlessly integrate single-shot

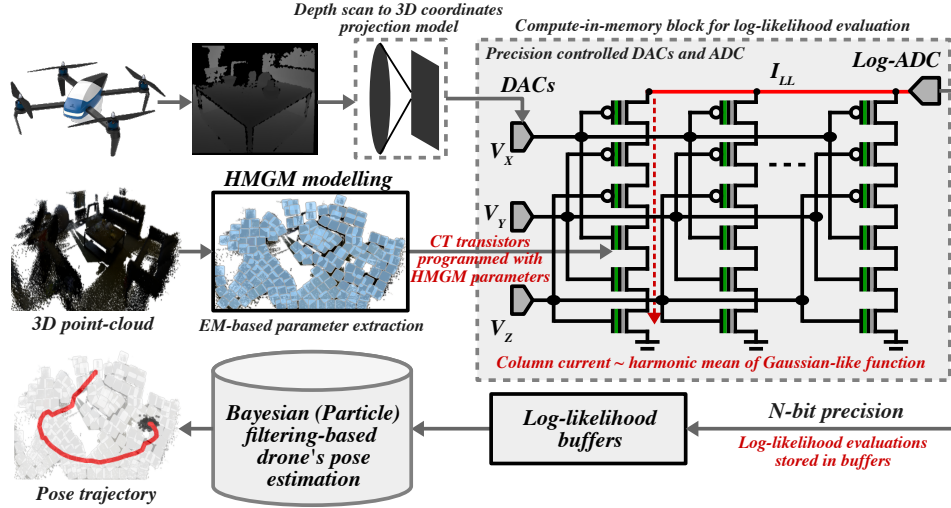


Fig. 2: Compute-in-memory based ultra-low-power Monte-Carlo localization framework for insect-scale drones. The framework inputs sequential depth projections. CIM is programmed with harmonic mean of “Gaussian-like” mixture (HMGMM) model parameters. CIM computes likelihood of depth measurements corresponding to hypothesized pose which is further used in particle filtering (PF) to predict pose of drone.

MLE/MAP estimates of drone poses as well as sequential localization steps (Bayesian filtering) as discussed above, the procedure can be quite computationally intensive. The most dominant complexity is the estimation of likelihood term  $P(\mathbf{z}|\mathbf{x})$  itself since the measurements (images/depth maps) are high dimensional and models correlating drone’s pose with the measurements can be quite complex depending on the size and intricacies of the 3D map.

A popular approach to extract  $P(\mathbf{z}|\mathbf{x})$  is by modeling the 3D map using a Gaussian mixture model (GMM) [22]–[24]. Using 3D scanning devices, such as Microsoft Kinect [25], [26], a point-cloud data-based 3D map of the domain can be captured. A GMM is synthesized to model the point-cloud data which essentially represents the density of “matter” in the 3D map. To adequately model intricacies of the 3D map, a sufficient number of mixture functions in the GMM are necessary. During flight, depth sensors in a drone capture a depth map of its current observation. Although, depth sensing is energy expensive, recent works such as [27], have shown energy efficient, small form-factor depth sensors, suited for insect-scale drones. Based on the current pose belief, the scan  $\mathbf{z}$  of  $N$  non-zero depth map pixels  $\{z_1, z_2, \dots, z_N\}$  is projected to 3D via the camera’s projection model:

$$\mathbf{C}_c = \begin{bmatrix} o_x + f \frac{C_x}{C_z} \\ o_y + f \frac{C_y}{C_z} \end{bmatrix} \quad (5a)$$

$$\mathbf{C}_w = [\mathbf{C}_c - \mathbf{T}_{cw}] \mathbf{R}_{cw}^{-1} \quad (5b)$$

Here,  $C_x$ ,  $C_y$  and  $C_z$  are the point coordinates in 3D space. Their 2D perspective projection in the camera frame is  $(f \frac{C_x}{C_z}, f \frac{C_y}{C_z})$ .  $C_c$  is the depth pixel coordinate matrix in camera frame mounted on the insect-scale drone.  $f$  is the focal length, and  $o_x$  and  $o_y$  are optical offsets.  $\mathbf{T}_{cw}$  and  $\mathbf{R}_{cw}$  are translation and rotation matrices, respectively, transforming depth scans in camera frame to the world frame based on the pose belief. Thereby,  $P(\mathbf{z}|\mathbf{x})$  is estimated by evaluating  $p_{\text{GMM}}(\mathbf{z}_{\text{proj}}(\mathbf{x}, \mathbf{z}); \Theta)$ , where  $\mathbf{z}_{\text{proj}}(\cdot)$  is the projection func-

tion of measurements  $\mathbf{z}$  to 3D space based on pose belief  $\mathbf{x}$ .  $\Theta$  are the GMM parameters.

In a typical evaluation of pose localization, the likelihood  $p_{\text{GMM}}(\mathbf{z}_{\text{proj}}(\mathbf{x}, \mathbf{z}); \Theta)$  is computed for hundreds of non-zero depth pixels and over hundreds of mixture functions in the GMM model. Therefore, the computational workload of  $P(\mathbf{z}|\mathbf{x})$  is excessive. Moreover, during a flight, the drone needs to continuously localize itself; hence, the timing constraints on  $P(\mathbf{z}|\mathbf{x})$  are also stringent. In the subsequent section, we discuss a novel approach to considerably minimize the energy demand for measurement likelihood evaluation which eventually leads to a viable low power probabilistic localization approach for insect-scale drones.

### III. ULTRA-LOW-POWER PROBABILISTIC LOCALIZATION

Prior works [22]–[24] use a GMM to probabilistically represent a 3D space, i.e., model the density of matter in the 3D map. However, evaluation of likelihood models based on GMM is computationally intensive. A dimension of each mixture function in GMM requires subtractions, multiplications, additions (to compute the exponent of a Gaussian function) as well as look-ups (to add exponents using a log-ADD table [28]–[30]). Since these operations are repeated on all dimensions, mixture functions as well as the hypotheses, likelihood evaluation of a typical depth map may require tens of thousands of arithmetic operations and hundreds of memory look ups to evaluate the likelihood of a single measurement.

#### A. A Mixture of Harmonic Mean of Gaussian-like Functions

We discuss a novel representation of 3D maps which can considerably simplify the computation of measurement likelihoods. Consider the six transistor inverter design controlled by three input voltages,  $V_x$ ,  $V_y$ , and  $V_z$ , in Figure 3(a). The transistors in the inverter comprise a floating gate to program threshold voltage [31]–[33]. Therefore, by programming the charge density in the floating gate, the threshold voltage of

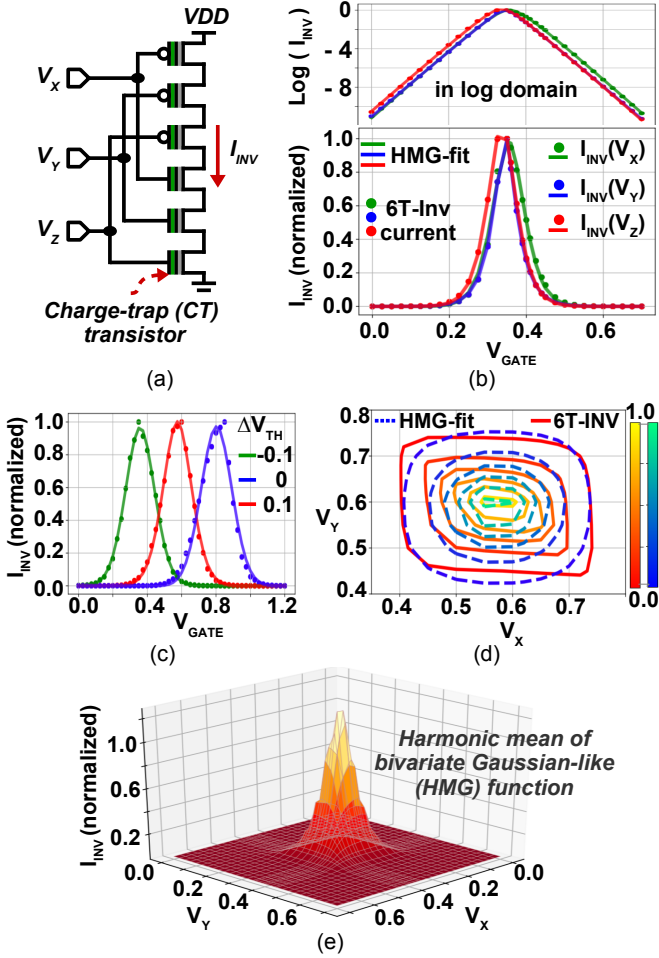


Fig. 3: (a) 6T-inverter circuit to emulate Harmonic mean of Gaussian-like (HMG) function. (b)  $I_{INV}$  behaves Gaussian-like upon varying one of the input voltages -  $V_X$ ,  $V_Y$ , or  $V_Z$ . (c) Programming  $I_{INV}$ -peak by controlling threshold voltage ( $\Delta V_{TH}$  in Volts). (d-e) Contour and surf plots with bi-variate input ( $V_X$ ,  $V_Y$ ) control.

transistors can be programmed in a non-volatile manner. In Figure 3(b), the inverter current,  $I_{INV}$ , through series-connected transistors emulates a Gaussian-like function. The figure shows  $I_{INV}$  when varying one of the input voltage -  $V_X$ ,  $V_Y$ , or  $V_Z$  - while keeping the others fixed.

Notably, the Gaussian-like nature of inverter's short circuit current can be understood by representative transistor's current equations. In Figure 3(b), close to the peak, inverter's short circuit current is governed by equating NMOS and PMOS current in the saturation regime, i.e.

$$I_{N,SAT} \approx \frac{\beta_n}{2} V_{dr,n}^2 (1 + \lambda_n V_{OUT}) \quad (6a)$$

$$I_{P,SAT} \approx \frac{\beta_p}{2} V_{dr,p}^2 (1 + \lambda_p (V_{DD} - V_{OUT})) \quad (6b)$$

Here,  $V_{dr,n} = V_{IN} - V_{TH,n}$  is NMOS's drive voltage and  $V_{dr,p} = V_{DD} - V_{IN} - V_{TH,p}$  is PMOS's drive voltage.  $V_{TH,n/p}$  is the threshold voltage of NMOS/PMOS,  $V_{IN}$  is the input voltage to the inverter,  $\lambda$  is the channel length modulation parameter, and  $\beta_n$  and  $\beta_p$  are the transconductance coefficients of NMOS and PMOS, respectively. Since  $I_{N,SAT} = I_{P,SAT}$ ,  $V_{OUT}$  and  $V_{IN}$  are related as

$$V_{OUT} \approx \frac{\beta_p V_{dr,p}^2 (1 + \lambda_p V_{DD}) - \beta_n V_{dr,n}^2}{\lambda_n \beta_n V_{dr,n}^2 + \lambda_p \beta_p V_{dr,p}^2} \quad (7)$$

Therefore, inverter's short circuit current near the peak is determined by applying  $V_{OUT}$  expression from (7) to (6a). Under the setting,  $\beta_p = \beta_n$  and negligible channel length modulation, inverter's current near the peak is given by

$$I_{INV,near\_peak} \approx \beta_n \frac{V_{dr,n}^2 V_{dr,p}^2}{V_{dr,n}^2 + V_{dr,p}^2} \quad (8)$$

Therefore, the peak current voltage,  $V_{peak}$ , is centered at  $V_{dr,n} = V_{dr,p}$ , i.e.,  $(V_{DD} + V_{TH,n} - V_{TH,p})/2$ . At  $V_{TH,n} = V_{TH,p}$ ,  $V_{peak}$  is at  $V_{DD}/2$ .  $V_{peak}$  can be modulated by  $\Delta$  amount by programming inverter's threshold voltages as  $V_{TH,n} \rightarrow V_{TH,n} + \Delta$  and  $V_{TH,p} \rightarrow V_{TH,p} - \Delta$ . Under these settings, the peak current magnitude is the same, and only  $V_{peak}$  modulates. Also, note that close to the peak,  $I_{INV,near\_peak}$  has a quadratic dependence to  $V_{IN}$ , just like a Gaussian function has to the input variable near its peak.

Away from the peak, inverter's current is governed by NMOS's (PMOS's) subthreshold current, i.e.,

$$I_{INV,tail} \approx I_{0,n} \exp\left(\frac{V_{dr,n}}{nV_T}\right) \quad (9)$$

Here,  $V_T$  is the thermal voltage and  $I_{0,n}$  is the leakage current at  $V_{dr,n} = 0$ . Therefore, at the tail, inverter's current decays exponentially. However, unlike in a Gaussian function, the exponent is linearly dependent on the argument variable ( $V_{IN}$ ). Therefore, we can model inverter's short circuit current using a "Gaussian-like" function defined as

$$I_{INV} \approx I_{0,INV} \exp\left(-\frac{(V_{IN} - \mu)^2}{\sigma^2(\alpha + |V_{IN} - \mu|)}\right) \quad (10)$$

Here,  $\mu$  is the input voltage where inverter's short circuit current peaks and depends on  $V_{TH,n}$  and  $V_{TH,p}$ .  $\alpha$  is a fitting parameter that models the transition from quadratic to exponential dependence of  $I_{INV}$  at increasing/decreasing  $V_{IN}$ .  $\sigma$  models the variance of  $I_{INV}$  and it depends on the thermal voltage and transistor's ideality factor,  $n$ . Figure 3(b) shows the correlation between the inverter current model in (10) and HSPICE-simulated inverter's short circuit current in linear and log-domains. Figure 3(c) shows the modulation of  $\mu$  by programming  $V_{TH,n}$  and  $V_{TH,p}$  in the inverter design.

Figures 3(d) and (e) show the contour and surface plots respectively of  $I_{INV}$  when varying two gate voltages at a time. Under a multivariate control of inverter's current, i.e., when more than one input voltages vary simultaneously, the characteristics of  $I_{INV}$  are, in fact, more closely represented by a Harmonic mean of Gaussian-like (HMG) function in (10) where each constituent 1D function is controlled by input  $V_X$ ,  $V_Y$ , and  $V_Z$ . The column current in the design follows a harmonic mean of Gaussian since the resistance of each inverter is inversely proportional to a Gaussian-like function. The column current can be expressed as

$$I_{INV} \approx \frac{I_{0,INV3D}}{\sum_{i=X,Y,Z} \exp\left(\frac{(V_i - \mu_i)^2}{\sigma^2(\alpha + |V_i - \mu_i|)}\right)} \quad (11)$$

Here,  $\mu_X$ ,  $\mu_Y$ , and  $\mu_Z$  are the respective mean of Gaussian-like functions which are controlled by the threshold voltage of transistors connected with the input voltage  $V_X$ ,  $V_Y$ , and  $V_Z$ , respectively.

Notably, compared to a multivariate Gaussian function, the implementation and evaluation of HMG in Figure 3 is much simplified. While a digital implementation to evaluate

---

**Algorithm 1: EM for HMGM representation.**


---

**Input:**  $\mathbf{d}_{pc}$  (Point-cloud co-ordinates)  
 $\Theta^{init}$  (Initial HMGM parameters)  
 $(\sigma$  and  $\alpha$  are tied to be same for all mixture components simplifying hardware complexity)  
 $\sigma$  (predetermined from inverter characteristics)  
 $\tau$  (EM tolerance)  
 $lr$  (Learning rate)  
 $N$  (Total point-cloud data points for EM)  
 $M$  (Number of HMGM components to learn)

**while**  $\Delta\mathcal{E} > \tau$  **do**  
  E-step:  
  **for**  $i = 1$  **to**  $N$  **do**  
    Compute:  
    **Membership probability**,  $\mathcal{M}(d_{pc}^i | \Theta^{(t)})$ :  
     $\mathcal{M}_0 = 0$   
    **for**  $j = 1$  **to**  $M$  **do**  
       $\mathcal{M}_j = \mathcal{M}_{j-1} + \lambda_j I_{INV}(d_{pc}^i; \mu_j, \sigma, \alpha)$   
       $I_{INV}(\cdot) \rightarrow$  expressed in (11)  
    **end**  
    **Expected log likelihood**:  
     $\ell(d_{pc}^i | \Theta^{(t)}) = \ell(d_{pc}^{i-1} | \Theta^{(t)}) + \ln \mathcal{M}(d_{pc}^i | \Theta^{(t)})$   
  **end**  
  Expectation,  $\mathcal{E}^{(t)} \equiv \ell(\mathbf{d}_{pc} | \Theta^{(t)})$   
  M-step:  
   $\Theta^{(t+1)} \equiv \arg \max_{\Theta} \ell(\mathbf{d}_{pc} | \Theta^{(t)})$   
**end**  
**Output:**  $\Theta^{optimal}$

---

multivariate Gaussian will require multiplier, adder, and lookup tables for exponential or log-ADD function [34], [35], HMG in Figure 3 is implemented using only six transistors and can be evaluated by applying analog voltages  $V_X$ ,  $V_Y$ , and  $V_Z$ . Also, compared to [36], the model can be implemented using typical CMOS transistors and doesn't require modifications in transistor design and processes. As we will discuss later, for drone localization,  $V_X$ ,  $V_Y$ , and  $V_Z$  will correspond to depth pixel's projection along 3D spatial dimensions. A model with mixtures of HMG functions can also be simply implemented by connecting many multi-input inverters in Figure 3(a) in parallel, each corresponding to a mixture component, and sharing their gate-input terminals. The total current from the parallel inverters will thus emulate the likelihood of measurements applied at the gates.

The likelihood of 3D projection of depth scan,  $\mathbf{d}_{meas}$ , for localization can, therefore, be computed using HMGM as

$$\ell(\mathbf{d}_{meas} | \Theta) = \sum_{i=1}^N \ln \sum_{j=1}^M \lambda_j I_{INV}(V_X^i, V_Y^i, V_Z^i; \mu_j, \sigma_j, \alpha_j) \quad (12)$$

Here,  $[V_X^i \ V_Y^i \ V_Z^i]$  is the 3D projection of  $i^{th}$  depth pixel to the world frame. Projection of depth scan to world frame was discussed in (5).  $\Theta$  represents the parameter set for HMGM, comprising of  $\lambda_i$  (mixing proportion),  $\mu_i$  (mean),  $\sigma_i$  (standard deviation) and  $\alpha_i$  (fitting parameter) for each respective mixture component  $i$ .

### B. Expectation-Maximization for HMGM

Parameters of HMGM ( $\Theta$ ) can be learned by adapting Expectation-Maximization (EM) [37] procedure as shown in Algorithm ???. We begin with randomly initializing  $\Theta$ . In the E-step, we compute the expected value of the log likelihood of 3D map's point cloud dataset  $\mathbf{d}_{pc}$ , i.e.,  $\ell(\mathbf{d}_{pc} | \Theta_t)$ . In the M-step, we compute optimal parameters  $\Theta^{(t+1)}$  that maximizes the expected log likelihood formulated in the E-step, i.e.,

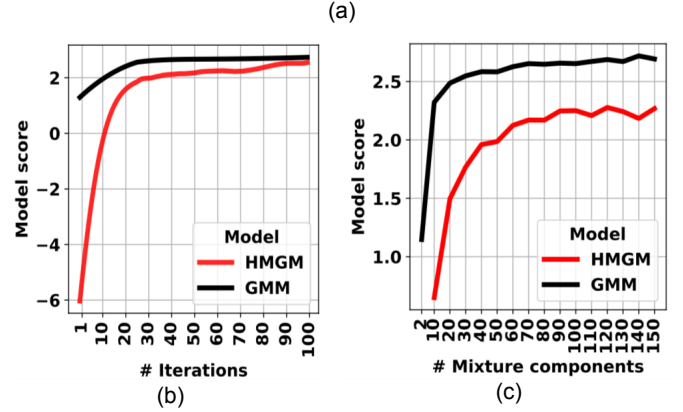
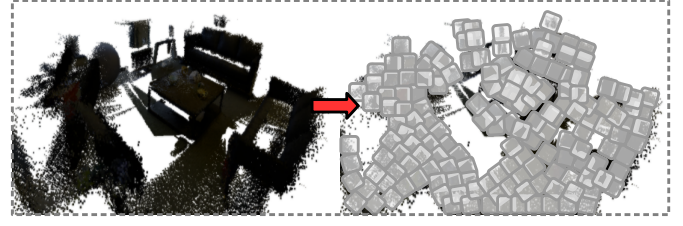


Fig. 4: (a) Harmonic mean of Gaussian-like mixture (HMGM) function representation of an indoor scene point-cloud. (b) Model scores of HMGM and GMM during Expectation-Maximization (EM) iterations to optimize model parameters over the point-cloud. (c) Model scores improve with increase in the number of mixture components.

$\Theta^{(t+1)} \equiv \arg \max_{\Theta} \ell(\mathbf{d}_{pc} | \Theta_t)$ . E-M steps are repeated until the log-likelihood of HMGM converges.

Under full programmability, variance  $\sigma_j$  of each mixture function can be learned independently. However, in our simplified implementation the variance of each mixture function is dictated by the technology and transistor parameters (width, length, etc). Conversely, the proposed scheme can easily implement a larger number of mixture functions with limited resource/power overhead. Therefore, we exploit a larger number of mixture components in our implementation to compensate for the lack of flexibility due to a tied variance. In Algorithm ??, only the mean and weights of mixture components are learned, therefore, and a predetermined  $\sigma$  based on 6T-inverter characteristics is used.

Figure 4(a) illustrates the fitting of Scene-1 in RGB-D dataset [38] using our HMGM-based model implemented through inverter array. We use “model score” to quantify the goodness of fit. The model score ( $\mathcal{MS}$ ) is evaluated as the average of HMGM function's value on point-cloud data,  $\mathbf{d}_{pc}$ , in the negative log-domain, i.e.,

$$\mathcal{MS} = -\frac{1}{N} \sum_{i=1}^N \ln \sum_{j=1}^M \lambda_j I_{INV}(\mathbf{d}_{pc}; \Theta^{(t)}) \quad (13)$$

A higher model score indicates a better representation of point-cloud data. Figure 4(b) shows that model score for HMGM increases with EM iterations and then plateaus. Figure 4(b) also shows the model score for GMM which shows similar fitting profile. In Figure 4(c), the model score is plotted at increasing number of mixture components for both HMGM and GMM models. The model score for both models improves with more mixture components and then plateaus. Although the model score of conventional GMM model is better than our HMGM model, the former model is much more complex



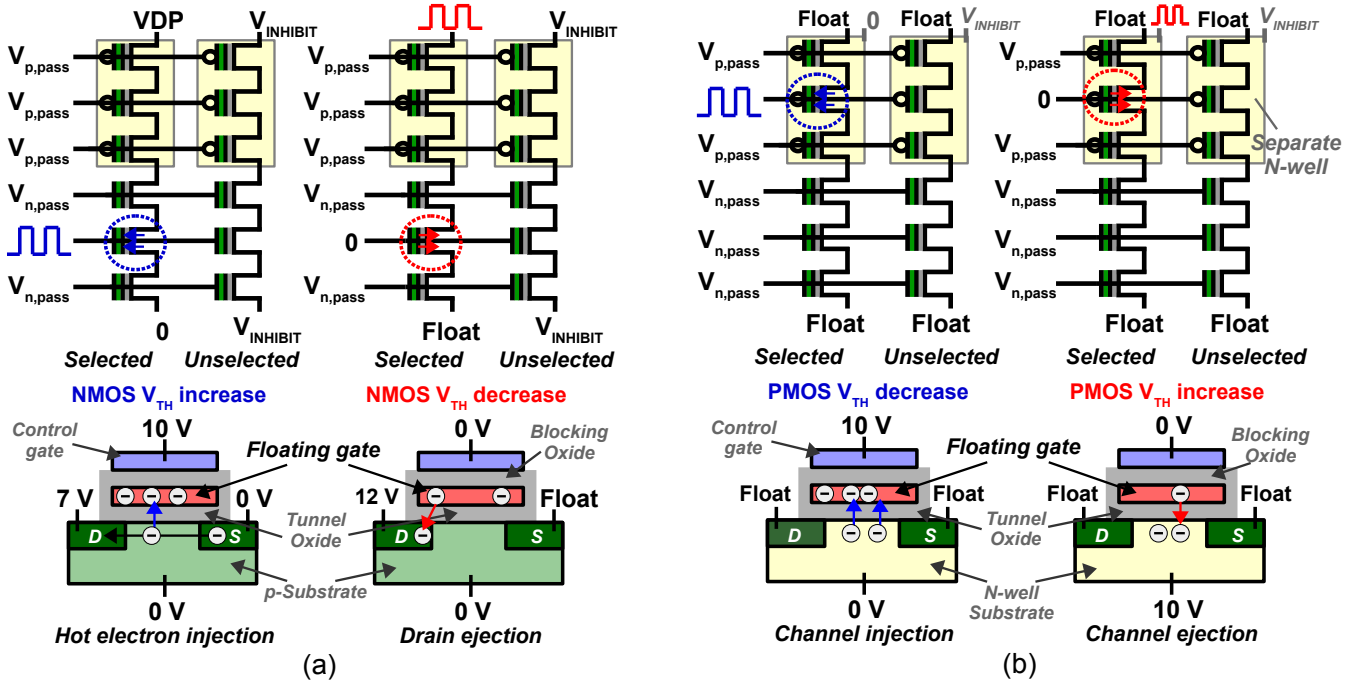


Fig. 6: Threshold voltage ( $V_{TH}$ ) programming in floating-gate inverter columns so as to program the mean of Harmonic mean of Gaussian-like mixture (HMGM) components. (a) Configuration to increase and decrease NMOS  $V_{TH}$ . (b) Configuration to increase and decrease PMOS  $V_{TH}$ .

Notably, PMOS's programmability in the above scheme requires separate n-wells for each column which affects the area efficiency of inverter array. However, this is not a critical concern for most applications since only a few thousand minimum-sized transistors are needed even for complex maps in our approach. Moreover, while our previous discussion considers floating gate CMOS for mean programmability, the schemes can also be extended to charge trap transistors (CTT). CTT based on  $HfO_2$ -metal gates were recently demonstrated [33], programmable under 2 V. Due to lower voltage operation, with CTT, the programming circuits of inverter array can be simplified to improve overall area efficiency of the array.

#### IV. CHARACTERIZATION ON BENCHMARK DATASET

We use three distinct scenes from the RGB-D Scenes Dataset v2 [38] to characterize our proposed localization framework. Each scene in the dataset is a 3D reconstructed point-cloud formed by aligning a set of video frames. The dataset also contains true camera poses for each frame. The camera pose constitutes the orientation expressed as quaternions ( $q, w, p, r$ ), and position as  $(x, y, z)$  coordinates.

We estimate drone's pose using the particle filtering (PF) approach under both global and relative localization. Under global localization, the drone is completely uncertain about its pose to begin with. By accumulating sequential depth measurements, the drone tracks its movements using PF. Under local localization, the drone is aware of the initial pose. However, since the motion model of drone is stochastic, it needs to track its movements based on depth measurements and a known initial pose as it navigates through the flying space. Under global localization, we initialize our PF setup with hundreds of hypothesized poses (i.e., particles) uniformly

distributed throughout the map. All particles (say  $K$  in number) are initialized with the same weight ( $1/K$ ) quantifying that each hypothesis is equally likely. We then project the scanned depth frame to 3D world coordinates based on a particle  $j$  using (5). Corresponding to each particle, a unique 3D projection of depth scan,  $d_{meas}^j$ , is determined. A model score  $\mathcal{MS}(d_{meas}^j | \Theta)$  for each particle-measurement pair is computed using our inverter array-based likelihood estimator in Figure 5. By accumulating model score of particles, their weights are updated as

$$w_j = \frac{\frac{1}{\mathcal{MS}(d_{meas}^j | \Theta)}}{\sum_{j=1}^K \frac{1}{\mathcal{MS}(d_{meas}^j | \Theta)}} \quad (15)$$

To eliminate less likely particles with each measurement, we resample them from the current particle set based on their weights while keeping the total number of particles same as  $K$ , similar to [42]. The weight-update followed by resampling results into an updated estimate of drone's pose with uncertainty in the pose illustrated by the variance of resampled particles. We then reassign equal weights to new particles and re-iterate all steps from weight-update till resampling for each subsequent depth scan. With this recursive Bayesian estimation, the particles eventually converge resulting into pose prediction with higher confidence. Figure 7 shows such particle filtering in action.

Figure 8 shows the trajectory tracking results on Scene-01 based on the approach. Figure 8(a) shows the point cloud map of Scene-01 along with sample RGB and depth scans from the drone. Figure 8(b) shows the trajectory tracking under global and relative localization for our approach and the conventional GMM-based approach. Notably, the tracking accuracy of our approach is similar to the conventional approach. Figure 8(c)

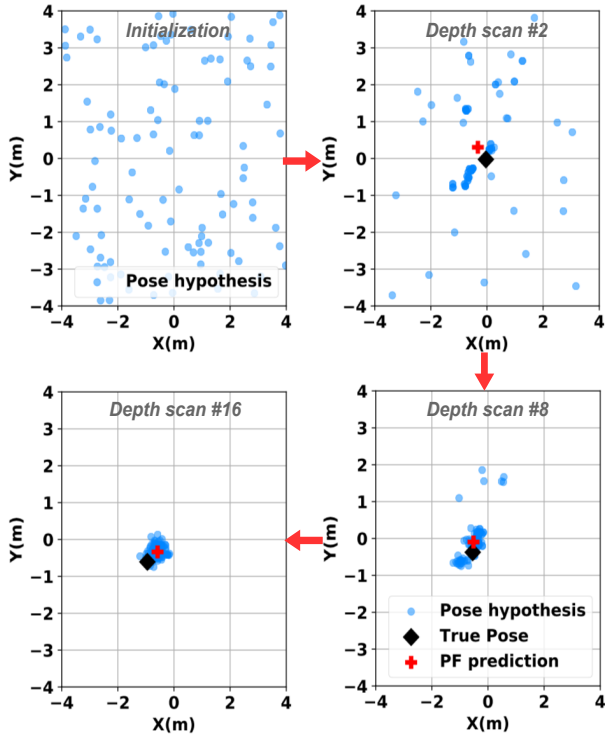


Fig. 7: Particle filtering (PF) on Scene-01 of RGB-D dataset using the proposed compute-in-memory (CIM) based HMGM model of the scene.

shows the confidence in pose estimation corresponding to every input depth frame. Under global localization, due to high initial uncertainty, variance bounds on pose particles are high. However, with each increasing measurement, the drone is able to minimize its uncertainty by particle filtering and using the proposed HMGM-based map representation. The bounds converge with subsequent scans illustrating improvement in prediction confidence. The error in position estimates is shown in Figure 8(d) with an upper error limit of  $\sim 0.8\text{m}$ . We also estimate drone’s pose by our localization framework on two more distinct scenes in the dataset, which are illustrated in Figure 9.

## V. IMPACT OF LOW PRECISION AND PROCESS VARIABILITY

We next analyze the implications of quantization on pose tracking of drone. The lower the operating precision, the lower is the area/power requirement which is critical for a drone with limited resource budget. However, excessively low precision can significantly degrade the accuracy of pose prediction. Figure 10 shows the impact of quantization of DAC, logarithmic-ADC and threshold (mean) programming on the pose estimation. DAC precision quantizes the 3D depth projection to inverter array, i.e.  $V_X$ ,  $V_Y$  and  $V_Z$ . Log-ADC precision quantizes the digitized log likelihood evaluated by the inverter array. Precision on transistor thresholds quantize the mean of HMGM mixture components and depends on the precision of floating gate memory in the inverter array. Compared to floating point precision, the root mean squared error (RMSE) of predicted poses at lower operating precision is higher as shown in the figure. Our simulation results indicate

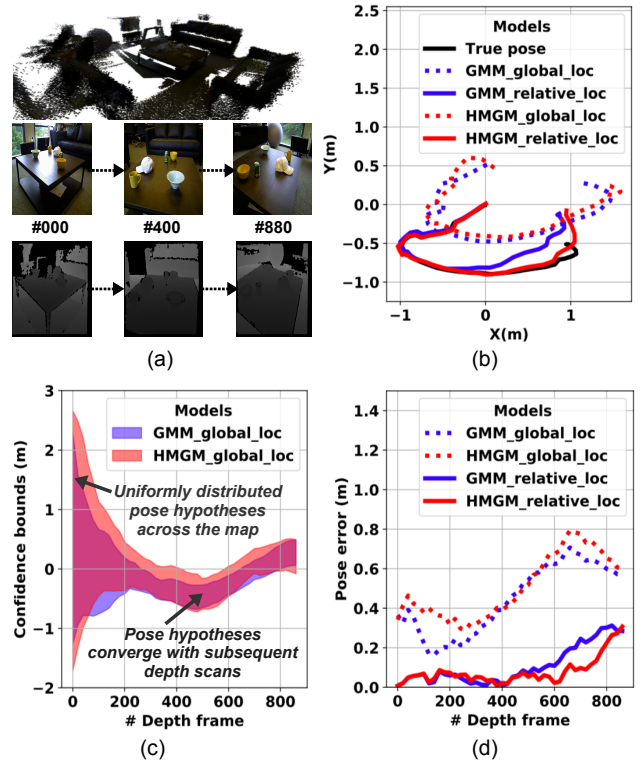


Fig. 8: Trajectory tracking results on (a) Scene-01 of RGB-D dataset. (b) Drone’s pose under both global and local (or relative) localization based on both HMGM and GMM. (c) Lower and upper bounds of pose hypotheses with sequential depth scans. (d) Pose error under both global and local localization.

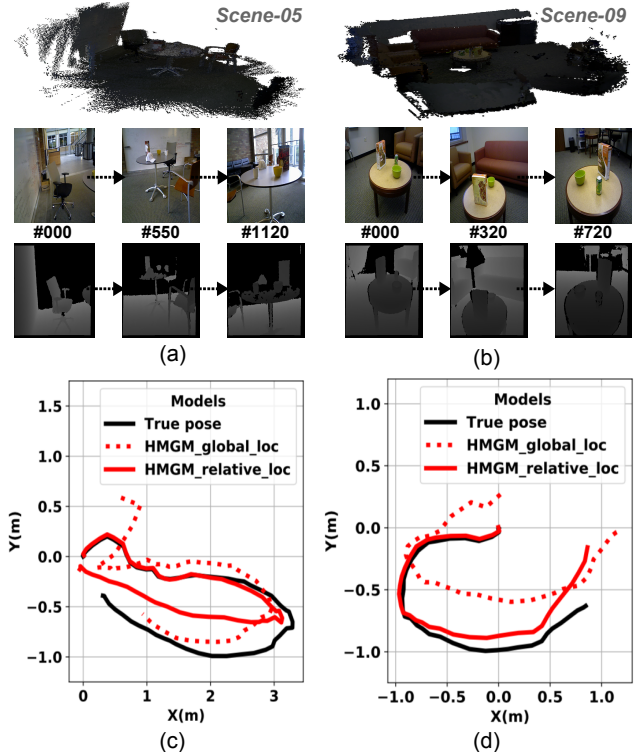


Fig. 9: Pose tracking results on (a, c) Scene-05, and (b, d) Scene-09 of RGB-D dataset under both global and local localization settings.

a non-monotonic change in RMSE at increasing precision, although, a higher precision generally helps in reducing RMSE.

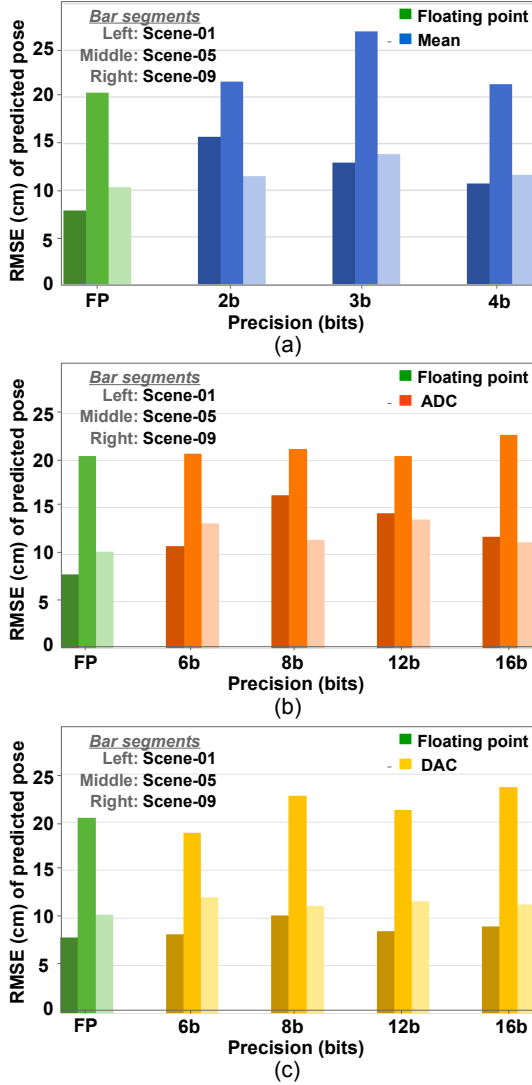


Fig. 10: Implications of low-precision (a) Mean, (b) ADC, and (c) DAC on pose prediction (root mean squared error (RMSE)) characterized over three distinct scenes of RGB-D dataset.

Nonetheless, even with very low precision in mean encoding, DAC, and ADC (such as 2-bit, 8-bit, and 8-bit, respectively), the pose estimation accuracy is competitive to the floating point precision.

We have also analyzed the impact of process variation on pose prediction in our approach, shown in Figure 11. Threshold voltage ( $V_{TH}$ ) variations in the inverter transistors degrade the emulation of 3D map model using inverter array, thereby, resulting in inaccuracy in likelihood evaluation and finally in pose estimation. The impact of  $V_{TH}$  variability is analyzed using Monte Carlo simulations.  $V_{TH}$  of transistors in the inverter array are randomly perturbed from the ideal based on process statistics of  $V_{TH}$  variability. For hundred random cases, RMSE of the predicted trajectories and ground truth is analyzed. Based on the simulation results in Figure 11,  $\sigma(V_{TH}) < 20$  mV is tolerable in our design and it does not degrade accuracy significantly from the baseline. Variations in  $V_{TH}$  of transistors can be controlled by increasing their sizes or process knobs such as reducing channel doping concentration.

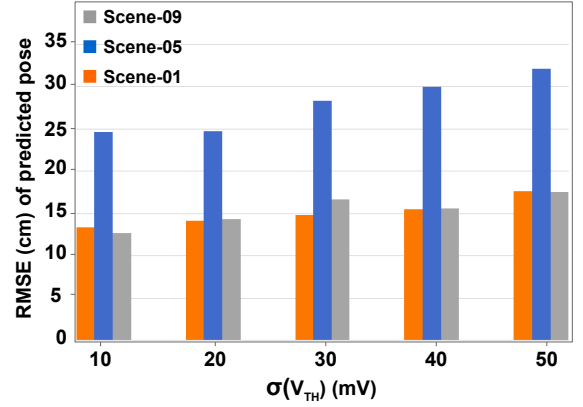


Fig. 11: Process variation analysis on pose prediction at three distinct scenes from RGB-D dataset illustrating RMSE vs variance in threshold voltage variation.

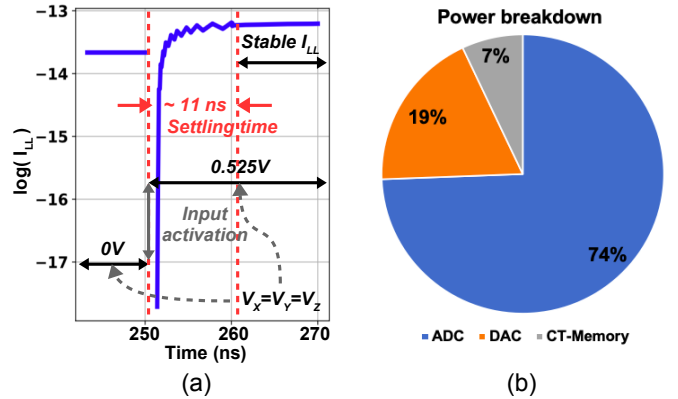


Fig. 12: (a) Floating gate CMOS memory latency to compute current-domain likelihood of a 3D depth-pixel projection. (b) Power breakdown of Floating gate CIM peripherals processing a depth frame over 100 pose hypotheses.

## VI. POWER-PERFORMANCE CHARACTERIZATION

We compute the power consumption and latency of our framework by processing  $640 \times 480$  pixels depth frame from the RGB-D scenes dataset described earlier. Figure 12(a) shows an example transient current profile from the inverter array when applying depth pixel's projection as a step input. The operation of inverter array takes about  $\sim 11$  ns to settle to a steady state value. Our considered 8-bit DAC requires  $\sim 15$  ns to convert measurements to analog domain and log-ADC digitizes its input activation in  $\sim 46$  ns. Thus, the total time to operate one depth pixel is  $\sim 72$  ns. Considering 100 particles in PF and on average  $\sim 60\%$  non-zero depth pixels (note that only non-zero depth pixels are projected and considered for likelihood evaluation), our framework takes  $\sim 1.33$  ms on average to process one depth frame. The statistics of non-zero depth pixels is based on the considered RGBD dataset. Therefore, even when as many as a thousand particles (hypotheses) are considered per input frame, our framework can operate at 75 fps (frames per second). Such high performance is enabled by parallel processing in the inverter array which processes all components of map representation model simultaneously.

Figure 12(b) shows the power breakdown for the measurement likelihood estimation in our approach. The total power consumption (with 100 inverter columns) for the likelihood

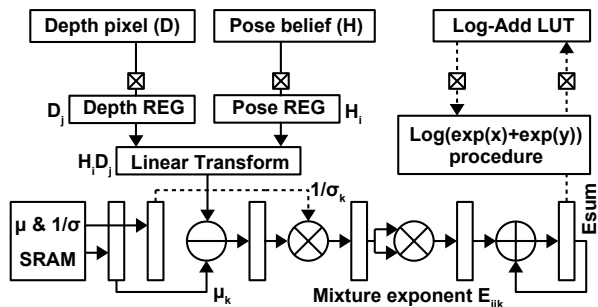


Fig. 13: Digital pipeline implementing Gaussian mixture model (GMM) for pose likelihood evaluation.

estimation is  $\sim 17 \mu W$  (at 45 nm CMOS process technology). We do not consider power contribution from the front-end digital processing to project depth pixels to the 3D space, since the workload for the likelihood estimations is the dominant component, exceeding by the orders of magnitude than the front-end processing. Log-ADC with several comparators and Op-Amps at multiple pipeline stages consumes 74% of the total power. The three DACs at the gate inputs contribute to 19% and the 100 column inverter array consumes 7% of the total power as shown in the figure. The power breakdown also indicates that with even more complex map representation model (i.e., the ones requiring more than 100 inverter columns to implement), the total power dissipation in our approach will not increase significantly from the current. To implement a more complex HMGM model, only more inverter columns will be needed and three DACs and one log-ADC will suffice as in the present configuration.

Figure 13 shows a comparative digital pipeline implementing a Gaussian mixture model (GMM) to evaluate likelihood of depth projections. We compare the performance of our framework with this digital pipeline implemented in 45 nm CMOS [43]. The pipeline consists of two multipliers, one adder, and one subtractor. The data flow is multiplexed for each tuple of depth pixel, particle (pose hypothesis), and GMM mixture component. Therefore, even to process one measurement, tens of thousands of iterations of the pipeline are needed. Due to such higher performance requirement, at the matching fps, the digital pipeline consumes  $\sim 7.6$  mW power which is  $\sim 450\times$  greater than our proposed FG-CIM framework. In our current estimate for the digital pipeline, we neglect the energy consumption for memory look-ups which will degrade the efficiency of conventional design even more compared to ours.

## VII. CONCLUSION

Energy efficient, low-latency, on-board processing of self-navigation algorithms is imperative in insect-scale drones. Our proposed floating-gate compute-in-memory (FG-CIM) framework performs confidence-aware localization of the drone with ultra-low-power consumption. The framework uniquely represents the domain map with 3D harmonic mean of “Gaussian-like” mixture (HMGM) density model, characteristic of the inverter columns that construct FG-CIM. The scalable design processes depth frames for large number of pose hypotheses at very high frames per second (FPS) due to massive parallelism,

paving the way for robust, ultra-low-power spatial intelligence in insect-sized drones.

## REFERENCES

- [1] A.-K. Mahlein, “Plant disease detection by imaging sensors—parallels and specific demands for precision agriculture and plant phenotyping,” *Plant disease*, vol. 100, no. 2, pp. 241–251, 2016.
- [2] N. Chebrolu, P. Lottes, T. Läbe, and C. Stachniss, “Robot localization based on aerial images for precision agriculture tasks in crop fields,” in *2019 International Conference on Robotics and Automation (ICRA)*. IEEE, 2019, pp. 1787–1793.
- [3] A. Kroll, W. Baez, and D. Peretzki, “On autonomous detection of pressured air and gas leaks using passive ir-thermography for mobile robot application,” in *2009 IEEE International Conference on Robotics and Automation*. IEEE, 2009, pp. 921–926.
- [4] C. Heyer, “Human-robot interaction and future industrial robotics applications,” in *2010 IEEE/RSJ International Conference on Intelligent Robots and Systems*. IEEE, 2010, pp. 4749–4754.
- [5] L. Aprville, T. Tanzi, and J.-L. Dugelay, “Autonomous drones for assisting rescue services within the context of natural disasters,” in *2014 XXXIth URSI General Assembly and Scientific Symposium (URSI GASS)*. IEEE, 2014, pp. 1–4.
- [6] E. T. Alotaibi, S. S. Alqefari, and A. Koubaa, “Lsar: Multi-uav collaboration for search and rescue missions,” *IEEE Access*, vol. 7, pp. 55 817–55 832, 2019.
- [7] V. K. KV, B. B. Khot, E. Oh, and B. Swain, “Home, office security, surveillance system using micro mobile drones and ip cameras,” Nov. 14 2017, uS Patent 9,819,911.
- [8] L. M. Belmonte, R. Morales, A. S. García, E. Segura, P. Novais, and A. Fernández-Caballero, “Assisting dependent people at home through autonomous unmanned aerial vehicles,” in *International Symposium on Ambient Intelligence*. Springer, 2019, pp. 216–223.
- [9] K. Y. Ma, P. Chirarattananon, S. B. Fuller, and R. J. Wood, “Controlled flight of a biologically inspired, insect-scale robot,” *Science*, vol. 340, no. 6132, pp. 603–607, 2013.
- [10] J. James, V. Iyer, Y. Chukewad, S. Gollakota, and S. B. Fuller, “Liftoff of a 190 mg laser-powered aerial vehicle: The lightest wireless robot to fly,” in *2018 IEEE International Conference on Robotics and Automation (ICRA)*. IEEE, 2018, pp. 1–8.
- [11] S. B. Fuller, “Four wings: An insect-sized aerial robot with steering ability and payload capacity for autonomy,” *IEEE Robotics and Automation Letters*, vol. 4, no. 2, pp. 570–577, 2019.
- [12] Y. M. Chukewad, J. James, A. Singh, and S. Fuller, “Roboffly: An insect-sized robot with simplified fabrication that is capable of flight, ground, and water surface locomotion,” *arXiv preprint arXiv:2001.02320*, 2020.
- [13] A. Suleiman, Z. Zhang, L. Carlone, S. Karaman, and V. Sze, “Navion: A fully integrated energy-efficient visual-inertial odometry accelerator for autonomous navigation of nano drones,” in *2018 IEEE Symposium on VLSI Circuits*. IEEE, 2018, pp. 133–134.
- [14] F. Mohammed, A. Idries, N. Mohamed, J. Al-Jaroodi, and I. Jawhar, “Uavs for smart cities: Opportunities and challenges,” in *2014 International Conference on Unmanned Aircraft Systems (ICUAS)*. IEEE, 2014, pp. 267–273.
- [15] R. M. Neal, *Bayesian learning for neural networks*. Springer Science & Business Media, 2012, vol. 118.
- [16] Z. Ghahramani, “Probabilistic machine learning and artificial intelligence,” *Nature*, vol. 521, no. 7553, pp. 452–459, 2015.
- [17] S. Thrun, “Probabilistic robotics,” *Communications of the ACM*, vol. 45, no. 3, pp. 52–57, 2002.
- [18] A. Kendall and R. Cipolla, “Modelling uncertainty in deep learning for camera relocalization,” in *2016 IEEE international conference on Robotics and Automation (ICRA)*. IEEE, 2016, pp. 4762–4769.
- [19] V. Fox, J. Hightower, L. Liao, D. Schulz, and G. Borriello, “Bayesian filtering for location estimation,” *IEEE pervasive computing*, vol. 2, no. 3, pp. 24–33, 2003.
- [20] F. Dellaert, D. Fox, W. Burgard, and S. Thrun, “Monte carlo localization for mobile robots,” in *Proceedings 1999 IEEE International Conference on Robotics and Automation (Cat. No. 99CH36288C)*, vol. 2. IEEE, 1999, pp. 1322–1328.
- [21] S. Thrun, “Particle filters in robotics,” in *Proceedings of the Eighteenth conference on Uncertainty in artificial intelligence*. Morgan Kaufmann Publishers Inc., 2002, pp. 511–518.
- [22] R. W. Wolcott and R. M. Eustice, “Fast lidar localization using multi-resolution gaussian mixture maps,” in *2015 IEEE international conference on robotics and automation (ICRA)*. IEEE, 2015, pp. 2814–2821.

- [23] A. Dhawale, K. Shaurya Shankar, and N. Michael, "Fast monte-carlo localization on aerial vehicles using approximate continuous belief representations," in *Proceedings of the IEEE Conference on Computer Vision and Pattern Recognition*, 2018, pp. 5851–5859.
- [24] H. Huang, H. Ye, Y. Sun, and M. Liu, "Gmmloc: Structure consistent visual localization with gaussian mixture models," *IEEE Robotics and Automation Letters*, vol. 5, no. 4, pp. 5043–5050, 2020.
- [25] Z. Zhang, "Microsoft kinect sensor and its effect," *IEEE multimedia*, vol. 19, no. 2, pp. 4–10, 2012.
- [26] R. B. Rusu and S. Cousins, "3d is here: Point cloud library (pcl)," in *2011 IEEE international conference on robotics and automation*. IEEE, 2011, pp. 1–4.
- [27] D. Wofk, F. Ma, T.-J. Yang, S. Karaman, and V. Sze, "Fastdepth: Fast monocular depth estimation on embedded systems," in *2019 International Conference on Robotics and Automation (ICRA)*. IEEE, 2019, pp. 6101–6108.
- [28] N. Iliev, A. Gianelli, and A. R. Trivedi, "Low power speaker identification by integrated clustering and gaussian mixture model scoring," *IEEE Embedded Systems Letters*, vol. 12, no. 1, pp. 9–12, 2019.
- [29] A. Gianelli, N. Iliev, S. Nasrin, M. Graziano, and A. R. Trivedi, "Low power speaker identification using look up-free gaussian mixture model in cmos," in *2019 IEEE Symposium in Low-Power and High-Speed Chips (COOL CHIPS)*. IEEE, 2019, pp. 1–3.
- [30] P. Shukla, A. Shylendra, T. Tulabandhula, and A. R. Trivedi, "Mc2ram: Markov chain monte carlo sampling in sram for fast bayesian inference," in *2020 IEEE International Symposium on Circuits and Systems (ISCAS)*, 2020, pp. 1–5.
- [31] F. Masuoka, M. Asano, H. Iwahashi, T. Komuro, and S. Tanaka, "A new flash e 2 prom cell using triple polysilicon technology," in *1984 International Electron Devices Meeting*. IEEE, 1984, pp. 464–467.
- [32] J. Y. Bak, M.-K. Ryu, S. H. K. Park, C. S. Hwang, and S. M. Yoon, "Nonvolatile charge-trap memory transistors with top-gate structure using in-ga-zn-o active channel and zno charge-trap layer," *IEEE Electron Device Letters*, vol. 35, no. 3, pp. 357–359, 2014.
- [33] F. Khan, E. Cartier, J. C. S. Woo, and S. S. Iyer, "Charge trap transistor (ctt): An embedded fully logic-compatible multiple-time programmable non-volatile memory element for high- $k$ -metal-gate cmos technologies," *IEEE Electron Device Letters*, vol. 38, no. 1, pp. 44–47, 2017.
- [34] A. Shylendra, S. H. Alizad, P. Shukla, and A. R. Trivedi, "Non-parametric statistical density function synthesizer and monte carlo sampler in cmos," in *2020 33rd International Conference on VLSI Design and 2020 19th International Conference on Embedded Systems (VLSID)*. IEEE, 2020, pp. 19–24.
- [35] A. Shylendra, P. Shukla, S. Mukhopadhyay, S. Bhunia, and A. R. Trivedi, "Low power unsupervised anomaly detection by nonparametric modeling of sensor statistics," *IEEE Transactions on Very Large Scale Integration (VLSI) Systems*, 2020.
- [36] A. R. Trivedi and A. Shylendra, "Ultralow power acoustic feature-scoring using gaussian iv transistors," in *Proceedings of the 55th Annual Design Automation Conference*, 2018, pp. 1–6.
- [37] T. K. Moon, "The expectation-maximization algorithm," *IEEE Signal processing magazine*, vol. 13, no. 6, pp. 47–60, 1996.
- [38] K. Lai, L. Bo, and D. Fox, "Unsupervised feature learning for 3d scene labeling," in *2014 IEEE International Conference on Robotics and Automation (ICRA)*. IEEE, 2014, pp. 3050–3057.
- [39] J. Lee, J. Kang, S. Park, J. Seo, J. Anders, J. Guilherme, and M. P. Flynn, "A 2.5 mw 80 db dr 36 db sndr 22 ms/s logarithmic pipeline adc," *IEEE Journal of Solid-State Circuits*, vol. 44, no. 10, pp. 2755–2765, 2009.
- [40] S. Aritome, *NAND flash memory technologies*. John Wiley & Sons, 2015.
- [41] E. Takeda, Y. Nakagome, H. Kume, and S. Asai, "New hot-carrier injection and device degradation in submicron mosfets," *IEE Proceedings I (Solid-State and Electron Devices)*, vol. 130, no. 3, pp. 144–150, 1983.
- [42] J. D. Hol, T. B. Schon, and F. Gustafsson, "On resampling algorithms for particle filters," in *2006 IEEE Nonlinear Statistical Signal Processing Workshop*, 2006, pp. 79–82.
- [43] Q. Xie, X. Lin, Y. Wang, S. Chen, M. J. Dousti, and M. Pedram, "Performance comparisons between 7-nm finfet and conventional bulk cmos standard cell libraries," *IEEE Transactions on Circuits and Systems II: Express Briefs*, vol. 62, no. 8, pp. 761–765, 2015.